Correspondence to:

L. Mantiloni,
lorenzo@gfz-potsdam.de

Author Contributions:

Conceptualization: L. Mantiloni, E. Rivalta, T. Davis
Data curation: L. Mantiloni
Formal analysis: L. Mantiloni
Funding acquisition: E. Rivalta
Investigation: E. Rivalta
Methodology: L. Mantiloni, E. Rivalta, T. Davis
Project Administration: E. Rivalta
Resources: E. Rivalta
Software: L. Mantiloni, T. Davis
Supervision: E. Rivalta
Validation: L. Mantiloni
Writing – original draft: L. Mantiloni, E. Rivalta

Mechanical Modeling of Pre-Eruptive Magma Propagation Scenarios at Calderas

L. Mantiloni[1,2] , E. Rivalta[1,3] , and T. Davis[4]

[1]Section 2.1 'Physics of Earthquakes and Volcanoes', GFZ German Research Centre for Geosciences, Potsdam, Germany, [2]Institute of Geosciences, University of Potsdam, Potsdam, Germany, [3]Department of Physics and Astronomy, Alma Mater Studiorum University of Bologna, Bologna, Italy, [4]Department of Earth Sciences, University of Oxford, Oxford, UK

Abstract Simulating magma propagation pathways requires both a well-calibrated model for the stress state of the volcano and models for dike advance within such a stress field. Here, we establish a framework for calculating computationally efficient and flexible magma propagation scenarios in the presence of caldera structures. We first develop a three-dimensional (3D) numerical model for the stress state at volcanoes with mild topography, including the stress induced by surface loads and unloading due to the formation of caldera depressions. Then, we introduce a new, simplified 3D model of dike propagation. Such a model captures the complexity of 3D magma trajectories with low running time, and can backtrack dikes from a vent to the magma storage region. We compare the new dike propagation model to a previously published 3D model. Finally, we employ the simplified model to produce shallow dike propagation scenarios for a set of synthetic caldera settings with increasingly complex topographies. The resulting synthetic magma pathways and eruptive vent locations broadly reproduce the variability observed in natural calderas.

Plain Language Summary Understanding the pathways that bring magma from an underground chamber to the surface helps to prepare for future eruptions in volcanic areas. Dikes are fractures filled with magma and represent the most common mechanism of magma transport in the Earth's crust. Their trajectories may be curved if the Earth's crust is deformed by the load of topography or by tectonic forces. Here we first discuss a model of such deformation processes in volcanic regions with complex but mild topography. Then, we develop a simplified dike propagation model that we compare to a more sophisticated one. Next, we combine our models and simulate magma pathways in artificially-generated scenarios.

1. Introduction

Geophysical observations of ground deformation and seismicity in volcanic areas have highlighted how some eruptions are preceded by a long phase of magma propagation in the form of magma-filled dikes (Cesca et al., 2020; Davis et al., 2021; Ebinger et al., 2010; Einarsson and Brandsdottir, 1980; Nakada et al., 2005; Patrick et al., 2020; Sigmundsson et al., 2015; Smittarello et al., 2022; Uhira et al., 2005; Wright et al., 2012). Some recent dikes have propagated for over 70 km, reaching locations that had not experienced any fissure opening in decades or centuries; in some cases the ensuing lava flows have resulted in massive property damage (Martí et al., 2022; Patrick et al., 2020) or loss of life (Smittarello et al., 2022). The associated dike trajectories have also displayed a variety of geometries, from horizontal to oblique to vertical, and shapes, from planar to segmented, curved or twisted (Bagnardi et al., 2013; Branca et al., 2003; Davis et al., 2021; Dumont et al., 2022; Martí et al., 2022; Patrick et al., 2020; Sigmundsson et al., 2015; Smittarello et al., 2022; Xu & Jónsson, 2014). In spite of the importance of this process, there are still no models to forecast, in three dimensions, the trajectory taken by magma during propagation in the shallow crust.

Our physical understanding of dike trajectories have progressed significantly in the last decades. Both early (Anderson, 1937) and more recent works (Dahm, 2000a) have established that dike pathways are largely determined by the balance between the elastic stresses in the host rock and the buoyancy force resulting from the density contrast between magma and rock. As a rule of thumb, dikes open against the direction of the least-compressive principal stress axis (A. Gudmundsson, 2002; Pollard et al., 2005; Ziv et al., 2000), while the combined effect of the external stress and the magma buoyancy force determines their direction of propagation (Pollard, 1987; Rivalta et al., 2015; Rubin, 1995; Taisne et al., 2011; M. R. Townsend et al., 2017; Weertman, 1971). The simplest two-dimensional (2D) trajectory models are streamlines perpendicular to the least-compressive stress

axis (Anderson, 1937; Pollard, 1987), while the most sophisticated approaches model dikes as cracks steered in the direction of maximum strain energy release rate (Dahm, 2000a; Maccaferri et al., 2010, 2011). Dike trajectory models have recently evolved from two-dimensional (Anderson, 1937; Dahm, 2000a; O. H. Muller & Pollard, 1977; Pollard, 1987) to partially (Heimisson et al., 2015; Pansino et al., 2022; Sigmundsson et al., 2015) or fully three-dimensional (3D) by Davis et al. (2020, 2021). The latter model extends to 3D the maximum strain energy release rate trajectory calculation approach introduced by Dahm (2000a); a 3D equivalent of the simple 2D streamline approaches is still missing.

The 3D model by Davis et al. (2020, 2021) has been applied to explain the counterintuitive trajectory of the 2018 dike at Sierra Negra, Galápagos. Importantly, Davis et al. (2021) confirmed the pivotal importance of a well-calibrated stress field in modeling dike trajectories: contributions from different stress-generating mechanisms, such as topographic gravitational loading and regional stress field, needed to be carefully adjusted in order to steer the dike on the observed trajectory. If we want to simulate 3D dike propagation at arbitrary volcanoes, we also need to determine their state of stress. This problem was addressed by Rivalta et al. (2019), who suggested a stress inversion strategy which involves, first, establishing the relevant sources of stress for the specific volcano, and then, tuning their relative intensity so that simulated dikes starting from the known location of magma storage reach the known locations of past eruptive vents. This strategy was tested on Campi Flegrei caldera in Italy, using only 2D (plane strain) stress models and 2D streamlines for dike propagation.

Extending the stress calibration strategy by Rivalta et al. (2019) to 3D would pave the way to forecast dike pathways in 3D at any arbitrary volcano. A preliminary step is to set up 3D stress and dike trajectory models that are computationally efficient for the large number of simulations needed by the stress calibration procedure. In this study, we first develop computationally efficient 3D stress field calculations for scenarios with topographic reliefs. Then, we develop a fast, semi-analytical 3D dike propagation model that approximates the sophisticated model by Davis et al. (2020, 2021) but retains the simplicity of 2D streamlines and can also backtrack a dike trajectory from eruptive vent to magma chamber. Finally, we show how to integrate all these models to produce realistic pre-eruptive magma propagation scenarios. We focus on calderas, setting up synthetic topographies inspired by natural systems.

2. Method Formulation

We assume a homogeneous, isotropic and linearly elastic medium as the host rock, described by rock density ρ_r, Young's modulus E and Poisson's ratio ν. g is the acceleration due to gravity. Symbols and parameters are defined in Table 1.

2.1. A Modular Approach to Understanding Stress States

We describe the state of stress within the host rock by a stress tensor σ_{ij}. Tensional stresses are positive. σ_{ij} is diagonalized to retrieve magnitudes, σ_1, σ_2, σ_3, from most compressive to least compressive, respectively, and eigenvectors, $\vec{v}_1$, $\vec{v}_2$, $\vec{v}_3$, which identify the orientations of the principal stress axes.

We build our 3D stress model following the first-order linear approach by Rivalta et al. (2019), who expressed the elastic stress field σ_{ij} of a volcanic region as the superposition of perturbations from a background stress state σ_{ij}^0, each stemming from a different stress-generating mechanism. The approach neglects coupling between the stress sources. We limit our analysis to tectonic stresses and gravitational loading/unloading because dike patterns can often be explained by a combination of the two mechanisms (Corbi et al., 2015; Heimisson et al., 2015; Maccaferri et al., 2017; Neri et al., 2018; Roman & Jaupart, 2014). Not including other mechanisms, such as pressurized magma reservoirs or faults, has the advantage of limiting the number of parameters in the model, while retaining the stress mechanisms with the largest influence. More contributions can be easily added, if needed in specific cases.

We write the stress tensor at any point in the crust as:

$$\sigma_{ij}(x, y, z) - \sigma_{ij}^0(z) = \sigma_{ij}^T + \sigma_{ij}^G(x, y, z) \tag{1}$$

where the terms on the right side arise, respectively, from the regional tectonic stress (T) and the gravitational loading/unloading (G).

Table 1
Parameters and Abbreviations of the Dike Propagation Model

Parameters		
Description	Symbol	Units
Host rock density	ρ_r	kg/m^3
Magma density	ρ_m	kg/m^3
Mode I stress intensity factor	K	Pa$\sqrt{m}$
Host rock fracture toughness	K_C	Pa$\sqrt{m}$
Young's modulus	E	Pa
Poisson's ratio	ν	
Dike radius	c	m
Number of observation points along the dike tip-line	n	
Backtracked dike radius	c_B	m

Description	Abbreviation
Forward dike trajectory	FT
Dike starting point	F_0
Dike surface	Σ
Observation points	$O_i, i = 1,\ldots,n$
Dike arrival point	F_A
Points defining dike trajectory	$F_i, i = 1,\ldots,A\text{-}1$
Projected dike arrival point	F_A^P
Backtracked dike trajectory	BT
Points defining backtracked trajectory	B_i
Backtracked dike starting point	BSP

The first step is to define the unperturbed state of stress, σ_{ij}^0, before any of the sources on the right hand side of Equation 1 became active. There are two main assumptions in literature: a laterally-confined medium, that is, no lateral strain can be produced after gravity is turned on (e.g., Martel & Muller, 2000; Savage et al., 1985), resulting in a vertical $\vec{v}_1$:

$$\sigma_{xx}^0 = \frac{\nu}{(1-\nu)}\rho_r g z, \quad \sigma_{yy}^0 = \frac{\nu}{(1-\nu)}\rho_r g z, \quad \sigma_{zz}^0 = \rho_r g z. \tag{2}$$

or a lithostatic stress state:

$$\sigma_{xx}^0 = \sigma_{yy}^0 = \sigma_{zz}^0 = \rho_r g z. \tag{3}$$

Field measurements of subsurface stress (Jaeger et al., 2007) lie somewhat in between those two assumptions. Therefore, σ_{ij}^0 can be written as:

$$\sigma_{xx}^0 = \sigma_{yy}^0 = k\rho_r g z, \quad \sigma_{zz}^0 = \rho_r g z, \tag{4}$$

where $k \in \left[\frac{\nu}{(1-\nu)}, 1\right]$ (Jaeger et al., 2007; J. R. Muller et al., 2001; Slim et al., 2015). In this study, we set $k = 1$ and assume a lithostatic unperturbed stress.

The second step is to superimpose the tectonic stress, expressed in terms of three independent components σ_{xx}^T, σ_{yy}^T, σ_{xy}^T, here assumed uniform (e.g., McKenzie, 1978; Müller et al., 1992).

The third step is to consider gravitational stresses associated to surface loading or unloading. This has often been modeled by distributions of normal forces onto a half-space (Dahm, 2000b; Maccaferri et al., 2014; Neri et al., 2018), which, however, neglect the shear stresses imposed by the topography and provide no information on the stress within the topography itself (McTigue & Mei, 1981). More sophisticated analytical solutions exist,

but are either 2D (McTigue & Mei, 1981; Savage et al., 1985) or only for simple topographies (McTigue & Mei, 1987). Stress due to surface loading/unloading decays over a vertical distance that scales with the radius of the topographic feature (e.g., Jaeger et al., 2007; Pollard et al., 2005; Roman & Jaupart, 2014). Consequently, principal stresses can change in both intensity and orientation over short distances. This has several implications discussed later (Section 2.2.1).

Martel and Muller (2000) and Slim et al. (2015) described how to implement topographic loads within Boundary Element (BE) models, where the topography is discretized into a mesh of dislocations. They considered the effect of topographic loading as akin to cutting an infinite body subject to gravity in two halves along a surface defined by the topography. The gravitational stress imposed by the upper half onto the lower one is then subtracted from the background stress of the body (Martel & Muller, 2000, Figure 3). In practice, this is achieved through imposing boundary conditions on the BEs, depending on the coordinate z of their midpoints and the rock density, which control the overburden or excavation pressure imposed by the topography.

One important point in models such as Martel and Muller (2000) is that the boundary conditions at the BEs representing the topography are univocally fixed only once the datum level, that is the unperturbed surface before any topography is created, is set. This was rarely clarified in past applications (e.g., Chadwick & Dieterich, 1995; Neri et al., 2018; Urbani et al., 2017). Identifying such surface is not always trivial but critical, as different choices lead to different outcomes for the displacement and stress field. We show this in Figure 1a, where we compare $\vec{v}_1$ from the analytical solution by McTigue and Mei (1981) for a valley adjacent to a ridge under plane strain assumption to 2D numerical models where the datum level is set to, successively, the flat extremes of the profile, the ridge summit and the valley bottom. The first model shares the same assumption on the datum level with the analytical solution, hence the good agreement for that case. Such assumption is straightforward to adopt when the topography becomes uniformly flat away from the loaded/unloaded region. However, this is not always the case, and the optimal choice of datum level may depend on the situation. Take, for example, a caldera lying on a coastline, which divides two regions, the mainland and the sea floor, at different elevations. We consider a similar case in our synthetic scenarios, and we solve the ambiguity in the datum level by setting it to the ground elevation before the caldera was formed: this coincides with the sea level in that case. If, for instance, we were to study the formation of an edifice and, later, of a caldera at its summit, we would first set the edifice datum level at its base, and then set the caldera datum level at the edifice summit. Consequently, the topography preceding the reference event (in our scenarios, the caldera formation) informs the datum level.

A further issue regarding the calculation of surface loading/unloading stresses is that they are not immutable. Volcanic regions host a variety of stress-generating and stress-relieving mechanisms acting on different time scales. For example, the build-up of a volcanic edifice consists of progressive accumulation of eruptive material that loads and stresses the underlying crust (McGuire & Pullen, 1989), while, at the same time, magmatic intrusions, earthquakes and inelastic processes tend to relax shear stresses and homogenize principal stresses (Chadwick & Dieterich, 1995). Quantifying stresses within large topographic loads at a particular point in time is thus non-trivial. Here we avoid this issue by focusing on calderas that we assume have formed relatively recently in the history of the volcano, and consider otherwise only mild topographies, so that modeling dike propagation within edifices is not necessary. We elaborate further on this point in Section 4. We note that when we use the term "caldera," we are referring to the general surface depression that is associated with all calderas. Differences in the origin, structure and setting of calderas (e.g., Acocella, 2007; Cole et al., 2005) are neglected.

We compute $\sigma_{ij}^G(x, y, z)$ in Equation 1 following Martel and Muller (2000), Slim et al. (2015). We employ the 3D BE tool *Cut & Displace* (Davis et al., 2017, 2019), based on the displacement discontinuity method by Crouch et al. (1983). We use *DistMesh* by Persson and Strang (2004) to discretize the topography into a mesh of triangular dislocations (Nikkhoo & Walter, 2015), acting as BEs. The 3D mesh needs to be larger than the region of interest, so that its edges are distant enough from the volume where we compute the stress. We find that a mesh with a diameter three times the lateral extent of the studied region is enough for that purpose, and we adopt this choice in all our models. If a coastline is present, the outer mesh tapers to two horizontal surfaces at different height, representing the far-field mainland and the far-field sea floor. Once the datum level is fixed, stress boundary conditions are imposed on each BE as previously described. The load imposed by the water column on the bathymetry is also included.

Calderas are usually filled with eruptive material or sediments over time (e.g., Hildreth et al., 2017; Orsi et al., 1996). Our model can account for this in several ways: the original buried caldera floor may be meshed as the reference topographic relief, and the corresponding BEs may be loaded accounting for the pressure deficit
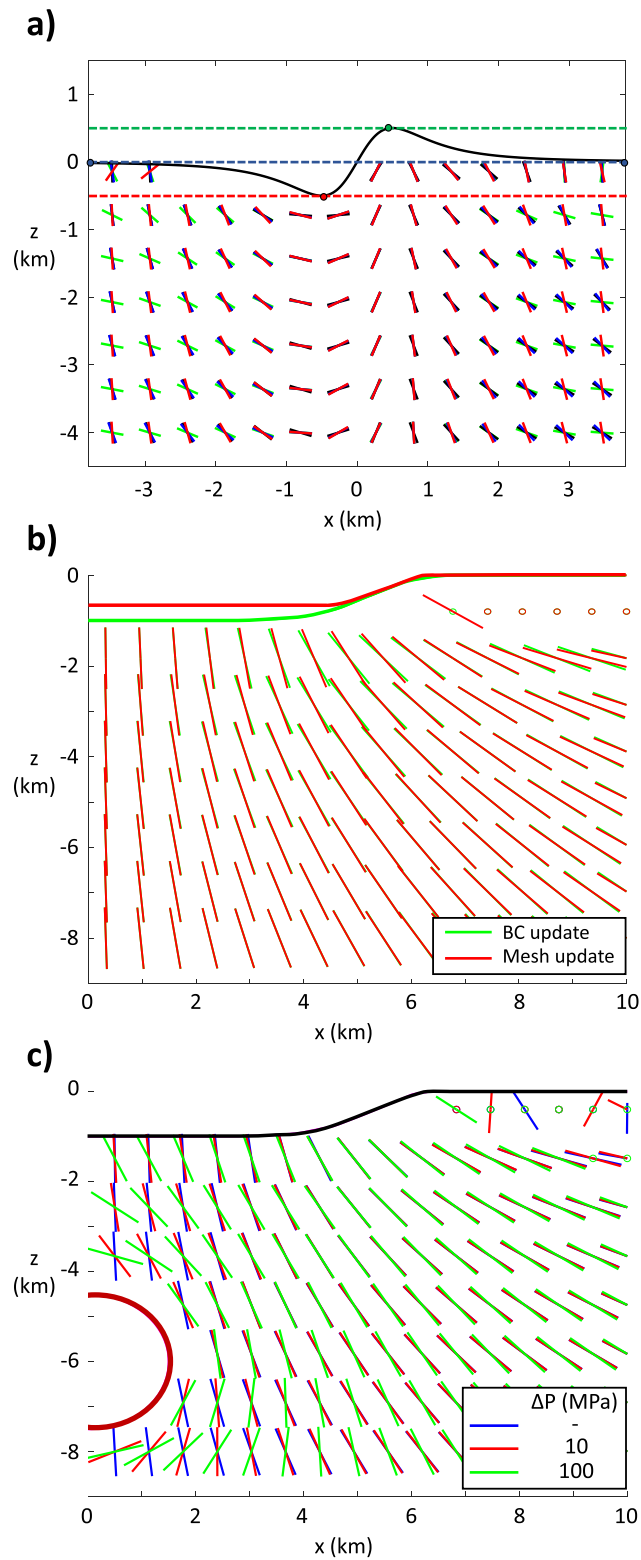
Figure 1.

due to the density contrast between the deeper host rock and the layers above. Alternatively, the current caldera topography may be meshed as the reference topographic relief, and the unloading pressure resulting from the missing mass due to lower density infill is factored in the boundary conditions. Calculations for these options for a synthetic caldera (Figure 1c) show good agreement except in the proximity of the caldera rim. Here we follow the former approach in one scenario, as illustrated later.

We remark that some of the stress sources we neglect, such as magma reservoirs, are in principle straightforward to include in our BE model. In order to show the minor relative influence of such sources, we compare in Figure 1b the orientation of $\vec{v}_3$ for three different models: one without and two with a pressurized, spherical magma chamber, with overpressure of 10 and 100 MPa, all involving the same surface unloading and tectonic stress. Only with extremely large overpressures the effects of the pressurization are felt at a distance of up to one source diameter. This validates in 3D a similar argument by Rivalta et al. (2019) (see their Figure 1).

2.2. Three-Dimensional Dike Propagation Model

2.2.1. Simplified Analytical Model (SAM)

Next, we develop a computationally-efficient 3D dike propagation model that provides a 3D equivalent to 2D $\vec{v}_3$-perpendicular streamlines. There is no straightforward method to compute streamlines in 3D, as the direction of $\vec{v}_3$ alone identifies a surface, while the direction of propagation on that surface remains undetermined. Davis et al. (2020, 2021) developed a point-wise, analytical dike trajectory calculator, similar to Sigmundsson et al. (2015) but fully 3D and more comprehensive in terms of factors considered. Its purpose was to justify why an observed dike took a specific direction depending on the magma buoyancy and the external state of stress, and falls short of being a propagation model. Here we turn that approach into a simplified 3D propagation model that can also backtrack dike trajectories downward from a vent to the magma storage region. We henceforth refer to our model as the "Simplified Analytical Model" (SAM).

In the analytical model by Davis et al. (2020, 2021), propagation of the tip-line of a dike occurs when the local mode I stress intensity factor, K, is larger than the fracture toughness, K_C, of the host rock (e.g., Secor & Pollard, 1975). The dike is represented as a tensile penny-shaped crack with a fixed volume, V, and radius, c. It is assumed that external stress varies linearly in every direction over the crack surface, and that internal pressure varies linearly with z proportional to $\rho_m g \sin\beta$, where β is the crack dip. In such case, K can be written as:

$$K = \frac{3\mu V}{4(1-\nu)c^2\sqrt{\pi c}} + \frac{4}{3\pi}\Delta\gamma^{max}c\sqrt{\pi c}\cos\alpha, \tag{5}$$

(Tada et al., 2000), where $\Delta\gamma^{max}$ is the maximum value over all orientations across the crack plane of the "pressure gradient", $\Delta\gamma$, calculated as the difference of the external stress and internal magma pressure over the crack diameter, and α is the angle spanning the circumference of the crack away from the direction of $\Delta\gamma^{max}$ (see Figure 2b). The second contribution in Equation 5, which is largest for $\alpha = 0$, determines the maximum of K and, thus, the direction of propagation of the crack. If $R_K = K/K_C > 1$, the crack propagates (see Figure 1 in Davis et al., 2020).

In SAM, we simplify such approach by forcing the dike to open against the local $\vec{v}_3$, and calculating K simply as

$$K = \frac{4}{3\pi}\Delta\gamma c\sqrt{\pi c}. \tag{6}$$

This is equivalent to neglecting the role played by the dike volume and K_C in determining whether the dike will advance. On the other hand, the buoyancy force contributes to $\Delta\gamma$, and plays a role in determining the direction of propagation on the $\vec{v}_3$-perpendicular surface.

In a Cartesian reference frame, where the z-axis is positive upward (Figure 2a), we calculate forward dike trajectories (FTs) as "paths of local steepest ascent," corresponding to the steepest increase of $\Delta\gamma$, as follows:

Figure 1. (a) Datum level choice: $\vec{v}_1$ orientation due to gravitational loading/unloading of a valley adjacent to a ridge (profile is drawn in black) under plane strain condition. The analytical solution by McTigue and Mei (1981) (black) is compared to our numerical solution with datum level fixed at the flat extremes of the topography (blue), the ridge summit (green) and the valley bottom (red). (b) Evolving topography: a 1-km-deep axisymmetric caldera is refilled by 1/3 of its original depth. $\vec{v}_3$ orientation and topographic profiles for two mechanically-equivalent models of caldera unloading with different reference topographic relief and boundary conditions. (c) Importance of reservoir: $\vec{v}_3$ orientation for three models involving a 1-km-deep axisymmetric caldera and vanishing tectonic stress. Two models include a 6-km-deep spherical magma reservoir of 1.5 km radius with overpressures $\Delta P = 10$ MPa (red) and 100 MPa (green) respectively; one has no reservoir (blue).
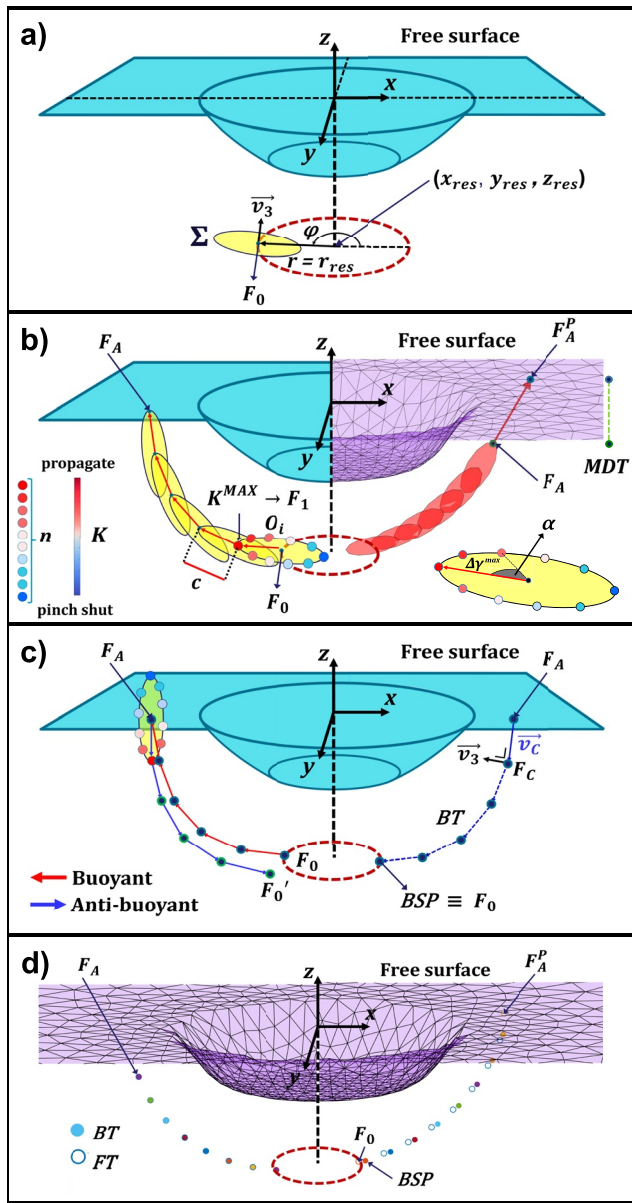
Figure 2. Simplified Analytical Model (SAM) framework. (a) reference systems employed throughout the work. Blue surface: simplified topography with a circular caldera. Red dotted line: edge of a magma storage region where the dike departs. Yellow surface: dike's initial surface (Σ). (b) Left: full SAM trajectory. Colored dots: observation points O_i; the colors are associated to K according to the colorbar. Right: Boundary Element mesh of the topography (vertically exaggerated) and actual foward trajectory (FT) from scenario "Circular-Caldera" (Section 2.3), extended until the free surface. Green dashed line on the right: minimum distance threshold. Bottom-right corner: O_i, direction of $\Delta\gamma^{max}$ (red arrow) and angle α away from $\Delta\gamma^{max}$ as defined in Equation 5. (c) Backtracking of SAM trajectories. Left: comparison between buoyant (red) and anti-buoyant (blue) trajectories. Right: representation of the backtracking algorithm outlined in Section 2.2.1. (d) Backtracked trajectories (BTs) of the FT shown in (b). Left: BT starts from the actual arrival point. Right: BT starts from the projected arrival point. Colored dots on both sides represent the BTs; empty blue dots the original FT.

1. We produce a stress model for the hosting medium (Section 2.1).
2. We choose a starting point F_0 for the dike (for instance, at the edge of a magma reservoir).
3. We compute σ_3 and $\vec{v}_3$ at F_0 and identify the local surface Σ perpendicular to $\vec{v}_3$. The dike is then defined as a penny-shaped crack of radius c lying on Σ (Figure 2a).
4. We generate a ring of n regularly-spaced observation points O_i, $i = 1...n$ along the dike tip-line (Figure 2b).
5. We calculate σ_3^i at each O_i and use it to calculate $\Delta\gamma$ for every point on the dike tip-line as:

$$\Delta\gamma_i = \frac{\left(\sigma_3^i - \sigma_3^j\right)}{2c} - \rho_m g \frac{\left(z_O^i - z_O^j\right)}{2c}, \tag{7}$$

where z_O^i, z_O^j are the vertical coordinates of points O_i, O_j, with O_j antipodal to O_i.

6. We calculate K^i at each O_i according to Equation 6 and determine the point F_1 where $K^i = K^{max}$. This will identify the direction of propagation of the dike (Figure 2b). Such direction coincides with that of the maximum pressure gradient across the plane of the crack. Note that negative K are always predicted at some O_i and imply unrealistic interpenetration of the crack faces. This poses no issue, however, since we are only interested in finding K^{max}.

We reiterate the previous steps taking F_1 as the current F_0 and produce a chain of points identifying the trajectory of the dike. The dike stops once at least one of the observation points generated in step 3 reaches a minimum distance threshold (MDT) between the observation points and the mesh, in order to prevent artifacts or singularities in the stress calculations. This is a characteristic issue of BE models, and can be mitigated with finer meshing (Slim et al., 2015). Here we fix the MDT to 800 m away from the nearest BE, as this is the average size of the dislocations of the mesh we employ. Dikes may be propagated past their F_A until they hit the surface at a "projected" arrival point, F_A^P, assuming that they maintain the dip and strike calculated at F_A (Figure 2b). This is akin to assuming that dikes do not have the space to adjust to the local stress field in the last ∼1 km before reaching the free surface. Moreover, a SAM dike is forced to stop if the trajectory becomes horizontal, or if the difference in the strike and dip angles between the current direction of propagation and the one at the previous step is larger than a given threshold. This prevents abrupt turning of the dike pathways.

SAM trajectories depend on two parameters, c and n. We found that values of n equal or greater than 12 lead to nearly identical dike pathways; we set n to 12 in all scenarios calculated later. In contrast, different c lead to different trajectories and arrival points for the same starting points and stress field. Large c (e.g., >2 km if the dike starting point is 10 km deep) sample the stress field in too few points and approximate $\Delta\gamma$ too coarsely to produce accurate trajectories, while very small c (e.g., <50 m for the starting depth mentioned above) follow principal stress directions nearly point-wise, but are more computationally expensive. We show later how c may be calibrated to better match a more sophisticated dike propagation model.

SAM also allows for the propagation of anti-buoyant dikes, that is, dikes filled with $\rho_m > \rho_r$ propagating downward through the crust. Dike trajectories, however, cannot be backtracked by simply inverting the density contrast between magma and rocks: an anti-buoyant dike starting from the arrival point of a buoyant one and propagating downward with the same c and n will

not pass through the same points (see Figure 2c), even if the difference between forward trajectories (FTs) and backtracked trajectories (BTs) decreases for smaller values of c.

We backtrack FTs, from known arrival points F_A and with assumed parameters c_B and n_B, as follows:

1. Starting from F_A, we find a candidate point B_C at a distance c_B such that the scalar product between $\vec{v}_3$ at B_C and the vector $\vec{v}_C$ pointing from B_C to F_A is minimal (Figure 2d).
2. We run one step of the forward model from B_C and calculate the vector between the predicted and actual F_A; we then shift B_C by that same vector and iterate this procedure until the desired precision is attained. B_C is taken as the first point B_1 of the BT.
3. The algorithm stops as soon as a specific requirement is satisfied: for instance, the current B_j falls within the known magma storage region. The lastly-recovered point of the BT becomes then the "backtracked starting point" (BSP) (Figure 2d).

The first step of the algorithm is modified when starting from a point F_A^P lying on the free surface, as we no longer fix the distance between B_C and F_A^P to a specific c_B, but let it vary over a specific range (for a FT with given c, we find a 0–3c range enough for our purpose).

We tested the method against known FTs, and found that it is able to retrieve each F_0 within a range of a few tens of meters (~0.2%–0.5% of a 6-km caldera radius) if starting from F_A, and a few hundreds (~2%–5% of the same caldera radius) if starting from F_A^P, provided the same radius c of the forward model is employed ($c_B = c$). If that is not the case, the distance between actual and BSP ($\Delta_{BSP} = |F_0 - BSP|$) increases with the difference between the backtrack radius c_B and c.

2.2.2. Three-Dimensional Intrusion Model (TIM)

We later validate SAM against the full-3D numerical dike propagation model by Davis et al. (2020) and Davis et al. (2021). The model needs the dike volume (V), assumed constant during the propagation. Here, the dike starts as a penny-shaped crack centered at a specific starting point and arranged according to a starting dip and strike; these can be either arbitrary or coincide with the local $\vec{v}_3$. The dike starting radius is taken as $c_0 = \sqrt{V/1.6\pi}$. The dike is meshed, and R_K is computed at every tip-line BE (Davis et al., 2019); the tip-line is advanced or retreated by an amount proportional to the local R_K, depending on its sign, and the crack is remeshed. The crack can also bend out of its plane according to the maximum circumferential stress criterion (Davis et al., 2021; Pollard et al., 2005). The dike can thus advance along complex trajectories and change its shape in the process. We refer to this model as "Three-dimensional Intrusion Model" (TIM).

TIM relies on finer discretization (at the scale of individual BEs) when calculating K. Comparing the two models is therefore critical to verify the validity of the approximations in SAM, especially at shallow depths, where even minor topographic features have a non-negligible influence and lead to more heterogeneous stress gradients (see Section 2.1).

Before comparing TIM and SAM trajectories, we illustrate how to combine the stress and dike models introduced so far into synthetic scenarios of dike propagation.

2.3. Configuration of the Dike Propagation Scenarios

We produce a total of nine synthetic scenarios (Tables 2 and 3). We first generate a stress model, evaluating which stress mechanisms are most relevant. Here, as discussed in Section 2.1, we limit our analysis to tectonic stresses and gravitational loading/unloading.

We consider increasingly complex topographies with a caldera located at the origin of the Cartesian reference frame (see Figure 2a). We employ four main topographic settings, each used in one or more scenarios:

- Setting 1: a flat topography with a circular caldera of radius $R_C = 6$ km and maximum depth $d = 500$ m. The depth of the caldera, which has steep slopes and a flat floor, varies with r according to:

$$z = -d \exp\left(-r^6\right) \tag{8}$$

- Setting 2: we add a coastline, modeled as a steep elevation step along the y-axis. In this way, we break the axial symmetry of the previous setting. The bathymetry lies 100 m below the datum level. The caldera has $R_C = 6$ km, $d = 450$ m, and depth varying with r as in (1).

Table 2
Modeled Scenarios

Scenario	Setting	N	d (m)	h (m)	σ_{xx}^T (MPa)	σ_{yy}^T (MPa)	σ_{xy}^T (MPa)	ρ_r (kg/m³)	r^{res} (km)	z^{res} (km)
Vertical-TIM	1	2 (2)	500	–	1	0	0	2,500	6	−6
Lateral-Dike	3	1 (0)	424	–	1	0.4	0	2,800	10.2	−6
Complex-Coastline	3	9 (9)	424	–	1	0.4	0	2,800	3	−6
Circular-Caldera	1	12 (12)	500	–	1	0.5	0	2,500	2	−6
Simplified-Coastline	2	24 (20)	450	–	1	1	0	2,500	2	−6
Tectonic-Shear	2	20 (10)	450	–	0.8	0.8	−1	2,500	2	−6
Refilling-Caldera	3–3b	20 (15)	424	–	1	0.4	0	2,800	3	−4
		20 (19)	221	–						
Two-Reservoirs	3	50 (39)	424	–	1	0.4	0	2,800	3	−4
									6	−8
Elliptic-Caldera	4	30 (26)	150	150	1	0.6	0	2,500	1	−6

Note. Columns are: chosen setting, number of SAM dikes (in parentheses, number of those reaching the MDT), caldera depth, resurgent dome height, tectonic stress components, host rock and reservoir parameters for each scenario. SAM, Simplified Analytical Model; MDT, minimum distance threshold.

- Setting 3: we maintain the bathymetry of (2), but we include two hills (heights 791 and 355 m, base diameter ~15 km). The caldera has $R_C = 6$ km and $d = 424$ m. The caldera shape is made irregular by adding Gaussian noise to Equation 8. In one scenario we model a topography evolving from (3) to (3b), where the caldera is partially refilled, its maximum depth changing to $d = 221$ m. This setting is inspired by the morphology of Campi Flegrei caldera.
- Setting 4: an elliptic caldera with $d = 150$ m, semi-major and semi-minor axes $a_C = 8$ km and $b_C = 4$ km, respectively. A circular resurgent dome with $h = 150$ m and 4.8 km diameter is located 3 km offset from the caldera center. The external topography has some gently-sloping hills (the maximum height is 157 m), but no bathymetry. This setting is inspired by the morphology of Long Valley caldera.

We calculate the gravitational loading/unloading as described in Section 2.1, using $E = 15$ GPa, $\nu = 0.25$ and setting ρ_r as in Table 3. Then, we superimpose to the resulting stress field the tectonic stress components σ_{ij}^T, different for each scenario.

Table 3
Parameters of Three-Dimensional Intrusion Model Dikes

Dike	V_k 10^6 m³	c_0^k (km)	ρ_m^k (kg/m³)
Vertical-TIM			
1	4	0.89	2,300
2	8	1.26	2,300
3	40	2.82	2,300
Lateral-Dike			
1	4	0.89	2,700
Complex-coastline			
1	2	0.63	2,300
2	10	1.41	2,250
3	9	1.34	2,100
4	5	0.99	2,280
5	4	0.89	2,350
6	3.5	0.83	2,300
7	3	0.77	2,270
8	3.8	0.87	2,390
9	2.4	0.69	2,300

Next, we choose a model of dike propagation and define the needed input. TIM needs dike volumes (V^k), magma densities $\left(\rho_m^k\right)$, K_C of the host rock and a starting geometry for the kth dike. We use $K_C = 70$ MPa·m$^{1/2}$. Starting dike radii (c_0^k) are determined by V^k (see Section 2.2.2 and Davis et al., 2021). SAM needs c and ρ_m.

We use the first three scenarios, "Vertical-TIM," "Lateral-Dike," and "Complex-Coastline," to compare the performance and features of TIM and SAM. In the additional six scenarios, we produce only SAM dike pathways with fixed $c = 1.2$ km and $\rho_m = 2,300$ kg/m³. We start with the most simplified topography ("Circular-Caldera"). Then, we progressively add new elements, such as a coastline ("Simplified-Coastline", "Tectonic-Shear"), hills and caldera refilling ("Refilling-Caldera", "Two-Reservoirs") and a resurgent dome ("Elliptic-Caldera"), studying their impact on dike trajectories. In three scenarios, the arrival points of SAM dikes are projected past the MDT to the free surface (see Section 2.2.1). All scenarios involve tensional stresses, whose principal axes coincide with the coordinate axes except for Tectonic-Shear (Table 2).

We fix the location, depth (z^{res}) and radius (r^{res}) of the magma reservoirs, which constitute the rock volumes where dikes depart from. We remark

that here the reservoirs have no contribution to the stress field. All magma reservoirs are circular, sill-like and centered at the origin of the reference frame. In Elliptic-Caldera, however, we consider a vertically-elongated reservoir centered below the summit of the resurgent dome.

The number of simulated dikes (N) varies among the scenarios (Table 2). Dike starting points are described by depth z_0^k, radius $r_0^k = r^{\text{res}}$ and angle ϕ_0^k, $k = 1,...,N$, according to the cylindrical reference frame in Figure 2a. In the most simplified scenarios, we assume equally-spaced starting points for dikes. In the most complex scenarios, we randomize the starting points by drawing ϕ_0^k from an uniform distribution. Starting depths coincide with the depth of the magma reservoir $\left(z_0^k = z^{\text{res}}\right)$, with two exceptions. In Two-Reservoirs, we consider two different starting depths, with the aim of representing two separate magma storage volumes. In Elliptic-Caldera, we draw z_0^k from a Beta distribution (e.g., Johnson et al., 1994) skewed toward the top of the reservoir (see Figure 5f). This is to simulate a case where dike nucleation probability may change with depth.

2.4. SAM and TIM Comparison

We now proceed to validate SAM against TIM to assess under which conditions the two models produce matching dike pathways. We use Vertical-TIM, which offers the simplest topography, and Lateral-Dike, which offers the most complex one, to compare TIM and SAM pathways under different starting conditions and settings. Then, we use Complex-Coastline to calibrate c in SAM.

If TIM dikes start misoriented with respect to the external stress field, they can progressively adjust to it as they advance, while SAM dikes start and remain perpendicular to $\vec{v}_3$. This can lead to discrepancies between SAM and TIM dike pathways. We show this in Vertical-TIM (Figure 3a), where three vertically-oriented TIM dikes with different volumes (V^k) and starting radii $\left(c_0^k\right)$ and two SAM dikes with different c propagate from the same starting point and with the same ρ_m (Table 3). In Figure 3a, TIM and SAM dikes first diverge, and later become roughly parallel, as TIM dikes adjust to the stress directions. Dikes with larger volumes require larger distances to do so, as already captured by 2D models (Dahm, 2000a; Maccaferri et al., 2010, 2019). We also notice how the SAM dike with the smallest c follow the stress field more closely.

In Lateral-Dike we show a situation where SAM captures 3D propagation as well as TIM. We run a TIM dike starting beneath a topographic high, and compare it to a SAM dike with radius $c = 1.2$ km starting from the same point. In this model, we set both dikes to be weakly buoyant ($\rho_r - \rho_m = 100$ kg/m³) and start aligned to the local stress directions. In these conditions (Tables 2 and 3), they both propagate laterally along similar trajectories, as dictated by the external stress and the low magma buoyancy: such behavior may not be captured by 2D dike models. In Figures 3e and 3f we observe that K values in SAM can be very different from the ones in TIM, and the SAM dike follows a longer, zigzagging pathway. This is due to the large c employed, which makes the dike advance too far to capture at each step the heterogeneity of the pressure gradient. Notwithstanding these differences, the overall directions of the pressure gradient (orange arrows in Figures 3e and 3f) are consistent, and the dikes follow each other closely even at shallow depths. In a test not reported here, we run the same scenario with a larger magma buoyancy ($\rho_m = 2,300$ kg/m³), and both TIM and SAM dikes ascended toward the free surface instead of propagating laterally. This shows how accounting for the magma buoyancy force in SAM makes it different from a simple "3D streamline" approach, as SAM dikes do not necessarily follow $\vec{v}_1$.

In Complex-Coastline (Figures 4a–4d), we study a case where TIM dikes start optimally-oriented (i.e., perpendicular to $\vec{v}_3$). We run nine TIM dikes with different V^k, c_0^k and ρ_m (Table 3), and compare them to forward SAM trajectories. Despite the V^k, c_0^k and ρ_m^k being different from one dike to another, the arrival points and final orientations of the SAM dikes are consistent with the outcomes of the TIM dikes, and SAM trajectories follow closely TIM ones. Such match is closest when we take $c = \bar{c}_0^k$, that is, the average of the c_0^k (Figure 4c).

In order to refine our calibration of c, we perform a comparison between TIM dikes and backtracked SAM dikes, evaluating how accurately their starting points are recovered with different values of backtrack radius c_B (Figures 4e and 4f). We find that the performance of our backtracking method in recovering the SP of the TIM dikes depends on the c_B we employ (see Table 1 for abbreviations). Both large (>1.2 km) and small (<0.6 km) c_B perform poorly. On the other hand, the distance between SP and BSP of each dike, Δ_{BSP}, is smallest for c_B equal or close to $\bar{c}_0^k = 880$ m (black vertical line in Figure 4e). The minimum of Δ_{BSP} for all dikes except for the one with the smallest V^k (Table 3) is found in the range 600 m $\leq c_B \leq 1$ km. A plot of c_0^k versus c_{best}^k, that is, the c_B
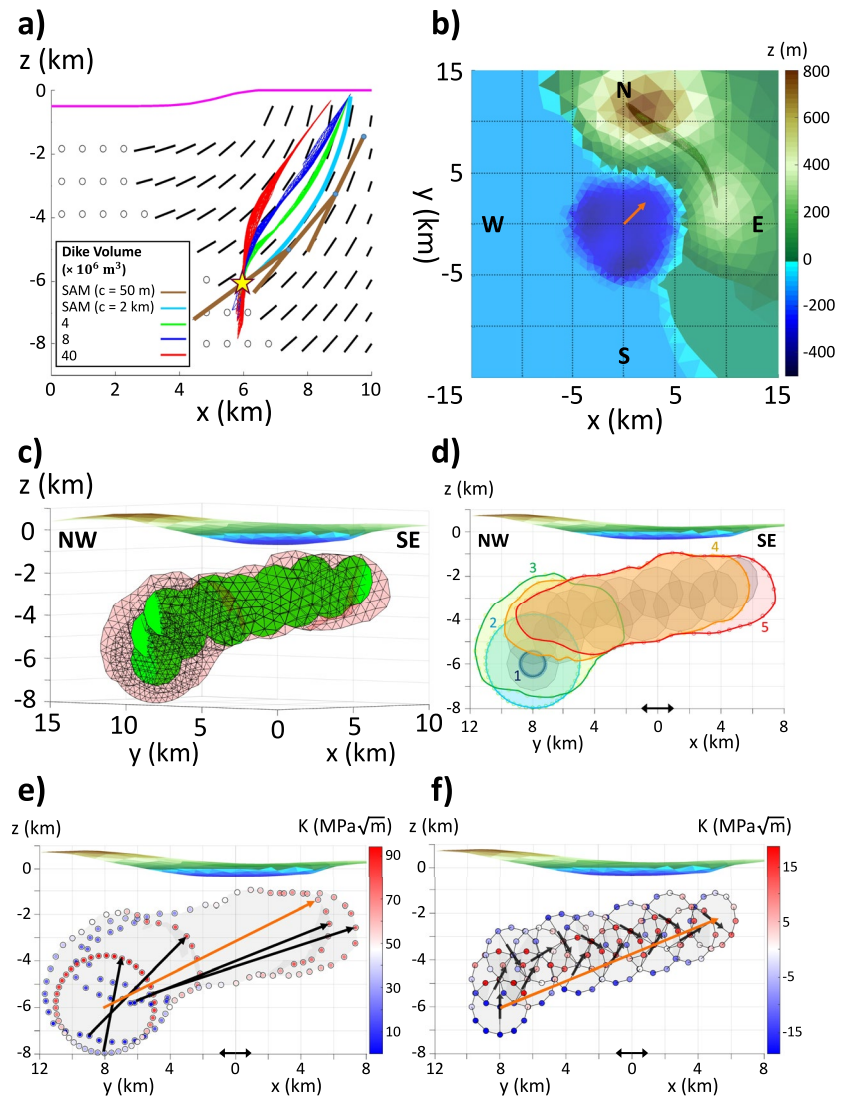
Figure 3. Three-dimensional Intrusion Model (TIM) and Simplified Analytical Model (SAM) comparison. (a) Vertical-TIM scenario: two SAM dikes with different c are compared to three TIM dikes with the same magma density and increasingly larger volumes. All dikes start from $x = 6$ km, $y = 0$ km, $z = -6$ km; TIM dikes are vertically-oriented at the starting point. TIM pathways are shown as meshes representing steps in dike propagation, including starting and final configuration of dike. Black segments show $\vec{v}_1$ projected over the x-z plane; black circles represent out-of-plane $\vec{v}_1$. Topography is represented as a magenta line. Blue dots mark the actual trajectory of SAM dike with largest c. (b) Lateral-Dike scenario: top view of topography of Setting 3, with TIM and SAM dikes propagating laterally beneath a topographic high. Both dikes start from $x = 2$ km, $y = 10$ km, $z = -6$ km, aligned to local $\vec{v}_3$. Color scale of topography is common throughout the Figure. (c) NW-SE view of (b) looking from the direction shown in (b) as an orange arrow. TIM dike represented as superposition of red meshes from five steps in the dike simulation, from start to end. Each step of SAM pathway is a green circle. (d) Outlines of the five steps of TIM pathway shown in (c). SAM cracks are superposed in gray. (e) Values of K computed along tip-line of TIM meshes, as well as K gradient directions for each step (black) and K gradient direction averaged over whole pathway (orange). Step 1 in (d) not shown here. (f) Values of K computed at observation points along tip-line of SAM cracks, as well as K gradient directions for each step (black) and K gradient direction averaged over whole pathway except for last step where dike stops (orange). For host rock and magma properties see Table 3.

leading to the most accurate BSP for the kth dike, shows that the best-fit line comes close to the bisector of the quadrant and, thus, $c_B = c_0^k = \sqrt{V^k/1.6\pi}$ provides a good estimate for the optimal radius c in SAM (Figure 4f).

In summary, SAM provides trajectories close to TIM dike trajectories only when the latter are well-oriented within the external stress field. In that case, the two models compare well even if the predicted values of K are very different. The optimal c for SAM may be chosen on the basis of the volumes of TIM dikes. The implication
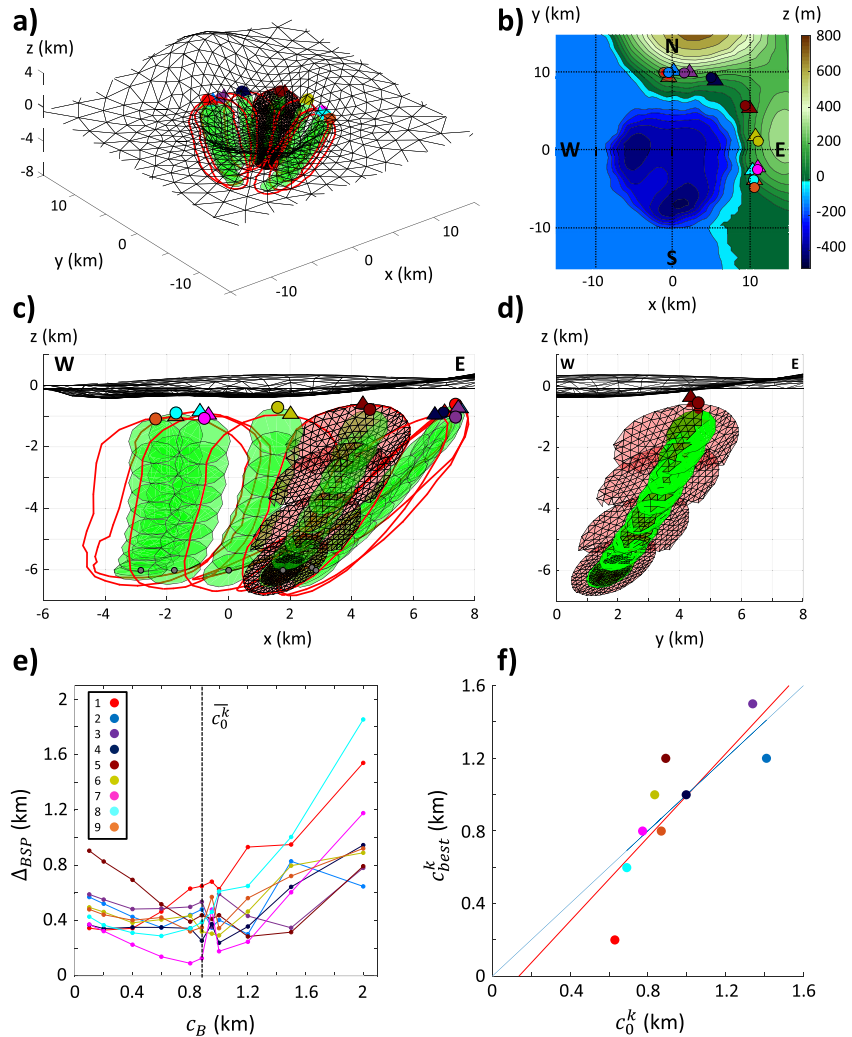
Figure 4. Complex-Coastline scenario. (a) Synthetic topography with a vertical exaggeration factor of 5, dike pathways (green for Simplified Analytical Model (SAM), red outlines for Three-dimensional Intrusion Model (TIM)) and arrival points of TIM (triangles) and SAM (dots) dikes. (b) elevation map and arrival points. (c) W-E view of TIM and SAM pathways, dike starting (gray dots) and arrival points. (d) detail of TIM and SAM pathways for the fifth dike. (e) SAM backtracking method applied to TIM pathways; distance between the actual and backtracked starting point Δ_{BSP} versus c_B (see Table 1). Black dotted line marks the average of c_0^k of TIM dikes. Colors are the same of TIM and SAM arrival points in (b) and (c), and numbers in the inset follow the order of Table 3. (f) c_{best}^k: c_B yielding the smallest Δ_{BSP} versus starting dike radius for each dike. The red line fitting the data is compared to the bisector (blue line).

is that, in a real scenario, knowledge on the volume of actual dikes could inform the choice of c for both forward and backward SAM. We add that, in Lateral-Dike, the running time of one step of SAM is ~100 times faster than that of one step of TIM.

3. Results

In the simplest model (Circular-Caldera, Figure 5a), dike trajectories are deflected by the gravitational unloading associated to the caldera, and their arrival points punctuate its rim. The tectonic extension is higher along the x-axis, and this leads to the spacing between neighboring arrival points becoming smaller when closer to that axis, even if the starting points are equally spaced.

In Simplified-Coastline, the presence of a coastline between two flat regions at different heights has an evident impact on dike trajectories, which are still deflected away from the caldera, but end up mostly on the mainland
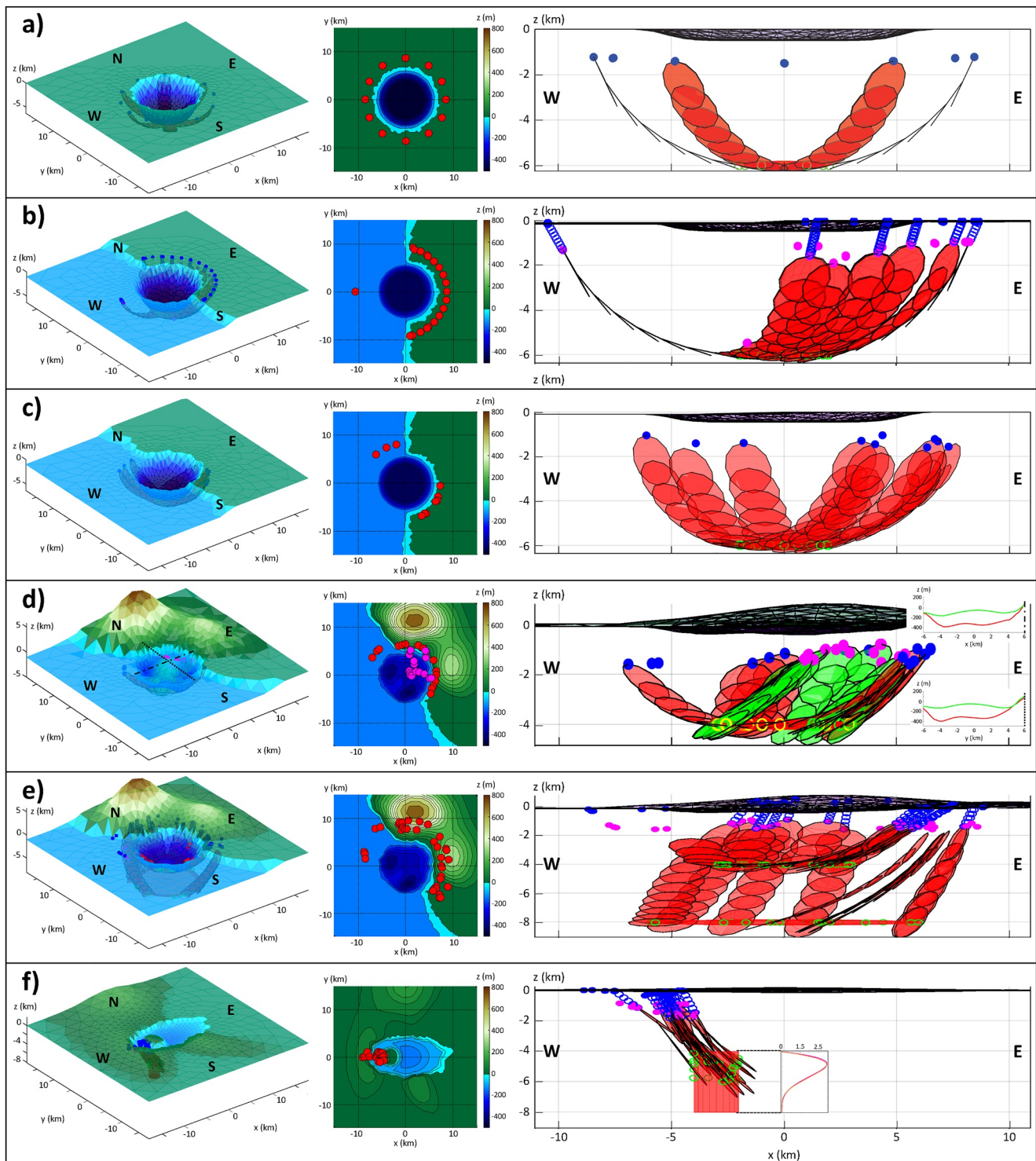
Figure 5.

(Figure 5b). Only the dike starting farthest away from the mainland manages to reach the sea floor. In particular, there is a concentration of arrival points close to the coastline. The effect of deviatoric tectonic stress is most apparent in Tectonic-Shear (Figure 5c). Here, the least-compressive principal tectonic stress axis roughly strikes along the bisector of the second and fourth quadrants (NW-SE). Arrival points cluster about such axis, both on the mainland and on the sea floor.

Caldera refilling and the presence of a resurgent dome cause an inward shift of dike trajectories. In Figure 5d (Refilling-Caldera), green dikes are still deflected by the caldera unloading, but all reach the surface along or within the caldera rim, some ending up on the resurgent dome. Topographic loads outside the caldera tend to attract dikes from both red and green sets.

Dikes departing from deeper storage regions, as in Two-Reservoirs (Figure 5e) show the same pattern as in the previous scenarios, reaching the surface farther away from the caldera.

Dikes in Elliptic-Caldera (Figure 5f) feel the competing influence of the elliptic caldera and the loading due to the resurgent dome and the hill west of the caldera. The synthetic vents cluster in two areas, the larger adjacent to the dome and the minor close to the caldera rim and the hill. No vents are present at the top of the dome.

In most scenarios, many dikes stop before reaching the MDT (Table 2) when the interplay between the buoyancy force and the external stress gradients is no longer sufficient to drive the dike upward. Dike arrest is often associated to gravitational loading (topographic highs): in Refilling-Caldera and Two-Reservoirs, most dikes ascending below the highest hills stop before reaching the MDT. This is consistent with the outcome of Lateral-Dike (Figures 3c and 3d), where both TIM and SAM dikes stop ascending and propagate laterally beneath a topographic load before stopping.

In summary, topography plays a dominant role in controlling dike pathways in our scenarios. Even relatively small topographic features, such as the ∼5-km-wide resurgent dome in Elliptic-Caldera (Figure 5f), influence close trajectories over a distance comparable to their width. In all scenarios, dikes are consistently deflected away from surface unloading and attracted by surface loading. Tectonic stress also influences dike orientation and clustering of arrival points, with a more evident impact in the simplest scenarios (Circular-Caldera, Simplified-Coastline, Tectonic-Shear).

4. Discussion and Conclusions

We have shown how our newly-developed "elementary" dike propagation model (SAM) well reproduces trajectories calculated with a sophisticated numerical model (TIM) by Davis et al. (2020); Davis et al. (2021) (Figures 3b,3c,3d, and 4), and can effectively model 3D dike pathways in synthetic calderas with tectonic stress and mild surface loading/unloading (Figure 5). In particular, SAM and TIM trajectories are similar if TIM dikes start optimally-oriented to the external principal stress directions (Figure 3a), since SAM dikes are always oriented perpendicularly to the local $\vec{v}_3$. Moreover, if stresses change over a distance smaller than c, the calculation of the pressure gradient (Section 2.2.1) and, consequently, SAM trajectories, will be more approximated. Large c values, however, are still reliable in our scenarios, since loads/unloads with large horizontal extent (>5 km) cause smoothly-changing stresses at the scale of most SAM dikes shown here (see Section 2.1). Loads/unloads of small extent (<1 km) would cause rapidly-changing stresses at that same scale, but their effect is significant only at shallow depths and can be neglected here, as we stop dikes at the MDT (Section 2.2.1). In this regard, fixing the MDT determines what topographic details are worth considering in our models. Dike propagation in both models is controlled not only by the gradients of external stress, but also by magma buoyancy. SAM is also able to backtrack dike trajectories from a vent to the magma storage region.

Due to our simplifying assumptions, our models have many potential limitations. The assumptions include homogeneous elastic parameters for the host rock. Rigidity and density layering may substantially affect dike propagation. For instance, dike trajectories can be deflected when crossing interfaces between layers with strong rigidity contrasts, as shown in 2D by Maccaferri et al. (2010). Further studies are needed to grasp the effects of layer interfaces in 3D. Nevertheless, as shown by Mantiloni et al. (2021) through analog experiments, homogeneous

Figure 5. Topography and selected Simplified Analytical Model dike trajectories for Circular-Caldera to Elliptic-Caldera scenarios. Left panels: synthetic topography and dike trajectories; central panels: elevation map and dike arrival points; right panels: W-E view of topography and dike trajectories. One out of two trajectories is shown for all scenarios, but all arrival points are displayed. (a) Circular-Caldera. (b) Simplified-Coastline. (c) Tectonic-Shear. (d) Refilling-Caldera: in left panel, both original and updated synthetic topographies are shown, with two cross-sections along x (dots and dashes) and y (fine dots) axes. Red dike trajectories are run with original topography, green ones with updated topography. In right panel, topographic profiles along respective cross-sections show original (red) and updated (green) topography. Magenta dots mark arrival points of dikes run with updated topography. (e) Two-Reservoirs. (f) Elliptic-Caldera: insets in right panel show the Beta distribution z_0^k are drawn from. General conventions as follows. Topography in left panels has a vertical exaggeration factor of 5. Dike starting and arrival points are represented as green circles and blue dots (red in elevation maps), respectively. In right panels of (b), (e), and (f), dike arrival points are magenta dots and blue circles are steps of projected dike trajectories to the free surface. Magma reservoirs: light-red volumes. Large-size versions of each panel may be found in Mantiloni et al. (2023).

models well reproduce the observed pathways provided that "effective" stress parameters are employed, rather than those actually imposed on the gelatin.

We also assume an elastic medium. Volcanic regions are known to host inelastic processes such as seismicity, damage, thermoplasticity, infiltration of and alteration by hydrothermal and magmatic fluids, that can affect both stresses and dike propagation. In particular, these inelastic processes compete with stress-generating mechanisms by homogenizing stresses (e.g., McGarr & Gay, 1978; Savage et al., 1992; Stephansson, 1988). Repeating magmatic intrusions may also bring the state of stress to isotropic in the long run: since they tend to open perpendicularly to $\vec{v}_3$, the strain they cause tends to bring σ_3 closer to σ_1 (Bagnardi et al., 2013; Chadwick & Dieterich, 1995; Corbi et al., 2015, 2016). Additionally, faulting and earthquakes may dissipate shear stresses over time. In other words, the stress contributions in Equation 1 can change or be altered. An accurate calibration of the stress state needs to take into account the relaxation of each stress contribution over time and space, discriminating between stress sources (in particular topography-altering events) that became active at different times. These processes are difficult to constrain and are currently accounted for through rough approximations. For instance, some works set the deviatoric stresses arising from gravitational loading of the edifice to zero (Davis et al., 2021; Heimisson et al., 2015). Corbi et al. (2015) found that superposing the effect of caldera unloading to a volcanic edifice where the state of stress is set to isotropic, rather than fully loaded, better explained the orientation of eruptive fissures at Fernandina, Galápagos. Here we neglected such processes by creating scenarios where dikes propagate below and around a caldera but not within an edifice, as the height of all topographic highs in our scenarios (Section 2.3) is lower than or comparable to the MDT (Section 2.2.1).

As shown in Figure 1c, stress contributions of magma reservoirs are dominant only in the proximity of the stress source. Such effect, nonetheless, can be important in determining nucleation points for dikes (Grosfils et al., 2015; A. Gudmundsson, 2006), that we do not model precisely here, as well as attracting or repelling incoming dikes if the reservoir pressure is increasing or decreasing, respectively (Pansino & Taisne, 2019).

Stress contributions due to previous large earthquakes may also deviate dikes or arrest their propagation. This has been considered both through theoretical (Maccaferri et al., 2014, 2016) and analog (Le Corvec et al., 2013) modeling. The fault-generated stresses do not influence dike trajectories significantly unless they come to close proximity (e.g., Maccaferri et al., 2014). However, Maccaferri et al. (2016) showed how an incoming dike can trigger the slipping of a pre-stressed fault, and be stopped by the resulting compressive stress. Faults and dikes may also interact with each other, for instance alternately accommodating tectonic extension (Gómez-Vasconcelos et al., 2020).

Lastly, the emplacement of dikes affects the local stress field as well, as both analytical (Rubin & Gillard, 1998) and numerical models (Ito & Martel, 2002) have shown. The interaction of dike intrusions can result in the deflection of subsequent dike trajectories (e.g., Kühn & Dahm, 2008; Takada, 1997), and may also dictate the architecture of reservoirs (Ferrante et al., 2022; Kühn & Dahm, 2008). Moreover, the cumulative effect of such interaction can modify the overall stress state (e.g., Cayol & Cornet, 1998).

All these stress sources can be integrated in our models as they stand now. Including stress mechanisms that are not well-constrained, however, ultimately adds more uncertainty to a model rather than improve it.

One major simplification in SAM is that of linear pressure gradients across the plane of SAM cracks (Section 2.2.1). SAM, as a simplified model, cannot deal with stresses that are too heterogeneous, although in the example shown in Lateral-Dike (Figures 3b–3d) it well compared to TIM, which can deal with stress heterogeneity at the scale of the individual triangular dislocations composing the dike meshes. An additional issue, not discussed here, is the potential heterogeneity in the dike internal pressure arising from the viscous flow of magma (Lister & Kerr, 1991) or pockets of bubble-rich magma within the dike (Costa et al., 2009). Non-linear gradients in the internal pressure may affect the direction of propagation of SAM dikes. In this regard, the analytical model by Pollard and Townsend (2018) computes the stress intensity factor at the tip of a 2D vertical crack under arbitrary distributions of normal tractions, and may be used in future works to estimate the error in K when using the linear pressure gradient assumption in SAM.

The outcomes of our synthetic scenarios show that dikes are deflected away from topographic lows (calderas), and attracted by topographic highs (hills, resurgent domes), even small-sized ones (e.g., the resurgent dome in Elliptic-Caldera). This is consistent with previous dike propagation and stress models considering topographic loading/unloading (Corbi et al., 2016; Dahm, 2000a; Rivalta et al., 2019; Roman & Jaupart, 2014) and with results

from gelatin-based analog models (Gaete et al., 2019; Mantiloni et al., 2021). The few synthetic scenarios we present here, however, are not designed to reproduce the wide variety of vent patterns observed at real calderas. They do, nonetheless, reproduce some common features of vent distribution in calderas. When a coastline is involved in our scenarios (Figures 5b–5e), most or all dikes end up on the mainland. This is compatible with vent patterns in similar natural settings, such as Campi Flegrei (Smith et al., 2011) or Aira caldera, Japan (Geshi et al., 2020). In our tests, no dike trajectories end up within the caldera, except in Refilling-Caldera and Elliptic-Caldera. Cases where past eruptive vents lie predominantly at or outside the caldera rim include most Galápagos volcanoes (Chadwick & Howard, 1991) and Aira caldera, Japan, (Geshi et al., 2020). Vents opening within a caldera can be observed in several other settings, like Newberry caldera, Oregon (MacLeod et al., 1982), Santorini caldera, Greece (Sigurdsson et al., 2006), or Campi Flegrei caldera, Italy (Smith et al., 2011). Intracaldera vent openings are predicted when the caldera is very shallow, unloading is reduced by refilling (Refilling-Caldera), or a resurgent dome is present (Elliptic-Caldera). Nonetheless, these factors are not always associated with intracaldera vents in nature (e.g., no eruptions have occurred at Long Valley caldera's resurgent dome after doming inception, Hildreth, 2004). Applying a model to a real caldera entails a deeper understanding of its evolution, stratigraphy and eruptive history, and requires dedicated work. For this reason, we chose not to apply our models to real calderas in this work, as running our model for a real scenario without a proper calibration of the stress state is no different than setting up a synthetic scenario with arbitrary stress. The fast dike propagation model we presented here is particularly suited for stress calibration procedures, such as the one by Rivalta et al. (2019). This will be the subject of future work.

Our model does not consider the viscous flow of magma within dikes and, as such, does not model dike velocity. The two approaches may be integrated by combining the pathways predicted by our model with existing models of dike velocity (Davis et al., 2023; Pinel et al., 2017) or growth, such as Zia and Lecampion (2020), introducing a numerical model of propagation of planar 3D hydraulic fractures, or Möri and Lecampion (2022); Pansino et al. (2022). We also remark that different magma compositions may involve large differences in magma viscosity and density, and neglecting the viscous flow may undermine the predictive power of our dike models in case of high-viscosity magmas.

In both SAM and TIM, dikes are assumed to break away from the magma reservoir after nucleation, as dike propagation is entirely driven by external stress and magma buoyancy force. In a more general case, the dike may be coupled to a reservoir, as past dike intrusion episodes have suggested (e.g., M. T. Gudmundsson et al., 2016; Maccaferri et al., 2016). The direction of dike propagation, however, may still be controlled by the gradient of internal pressure and external stress rather than the pressure imparted by the chamber, even though accounting for the viscous flow may change that. Analytical models of propagating dikes coupled with a magma chamber (Segall et al., 2001; Rivalta, 2010; M. Townsend & Huber, 2020) are only available for fixed dike orientations and, as such, cannot be applied to 3D dike trajectories. In our context, increasing the volume of a TIM dike as it advances could be a rough approximation of a dike-magma chamber coupling. Our results from comparing TIM and SAM (Section 2.4) suggest that the trajectories would not differ much even for large volumes of TIM dikes, as long as they start aligned to the external stress field (see Figures 3a, 4a, and 4c). Including dike-reservoir coupling in SAM or TIM, however, requires dedicated work.

In conclusion, we have developed a fast and flexible dike propagation model, complementing the numerical model by Davis et al. (2020, 2021) Stress models, however, are still critical and not yet fully understood. In a real-case application, our scenarios would be the end point of a stress calibration, whereby the stress state of a volcanic region is constrained through a statistical procedure aiming at matching dike simulations with observations, such as past vent locations (Rivalta et al., 2019), orientation of exposed dikes (Maerten et al., 2022) or focal mechanisms (Zhan et al., 2022). Our model is well-suited for such purpose. Once the stress is calibrated, it may be used to perform a long-term forecast on future vent locations, while the more sophisticated model may be employed to produce short-term propagation scenarios for incipient dike intrusions.

Data Availability Statement

The open-source software *DistMesh* is found at http://persson.berkeley.edu/distmesh/. The open-source Boundary-Element tool *Cut & Displace* is found at https://doi.org/10.5281/zenodo.3694164. The open-source Julia code used for TIM is found at https://doi.org/10.5281/zenodo.4726796 and https://doi.org/10.5281/

zenodo.4727208. The code for SAM and the data of the synthetic scenarios are available at https://doi.org/10.5880/GFZ.2.1.2023.001 (Mantiloni et al., 2023).

References

Acocella, V. (2007). Understanding caldera structure and development: An overview of analogue models compared to natural calderas. *Earth-Science Reviews*, *85*(3–4), 125–160. https://doi.org/10.1016/j.earscirev.2007.08.004

Anderson, E. M. (1937). Ix.—The dynamics of the formation of cone-sheets, ring-dykes, and caldron-subsidences. *Proceedings of the Royal Society of Edinburgh*, *56*, 128–157. https://doi.org/10.1017/s0370164600014954

Bagnardi, M., Amelung, F., & Poland, M. P. (2013). A new model for the growth of basaltic shields based on deformation of Fernandina volcano, Galápagos Islands. *Earth and Planetary Science Letters*, *377*, 358–366. https://doi.org/10.1016/j.epsl.2013.07.016

Branca, S., Carbone, D., & Greco, F. (2003). Intrusive mechanism of the 2002 NE-Rift eruption at Mt. Etna (Italy) inferred through continuous microgravity data and volcanological evidences. *Geophysical Research Letters*, *30*(20), 2077. https://doi.org/10.1029/2003gl018250

Cayol, V., & Cornet, F. H. (1998). Three-dimensional modeling of the 1983–1984 eruption at Piton de la Fournaise Volcano, Réunion Island. *Journal of Geophysical Research*, *103*(B8), 18025–18037. https://doi.org/10.1029/98jb00201

Cesca, S., Letort, J., Razafindrakoto, H. N., Heimann, S., Rivalta, E., Isken, M. P., et al. (2020). Drainage of a deep magma reservoir near Mayotte inferred from seismicity and deformation. *Nature Geoscience*, *13*(1), 87–93. https://doi.org/10.1038/s41561-019-0505-5

Chadwick, W. W., & Dieterich, J. H. (1995). Mechanical modeling of circumferential and radial dike intrusion on Galapagos volcanoes. *Journal of Volcanology and Geothermal Research*, *66*(1–4), 37–52. https://doi.org/10.1016/0377-0273(94)00060-t

Chadwick, W. W., & Howard, K. A. (1991). The pattern of circumferential and radial eruptive fissures on the volcanoes of Fernandina and Isabela islands, Galapagos. *Bulletin of Volcanology*, *53*(4), 259–275. https://doi.org/10.1007/bf00414523

Cole, J., Milner, D., & Spinks, K. (2005). Calderas and caldera structures: A review. *Earth-Science Reviews*, *69*(1–2), 1–26. https://doi.org/10.1016/j.earscirev.2004.06.004

Corbi, F., Rivalta, E., Pinel, V., Maccaferri, F., & Acocella, V. (2016). Understanding the link between circumferential dikes and eruptive fissures around calderas based on numerical and analog models. *Geophysical Research Letters*, *43*(12), 6212–6219. https://doi.org/10.1002/2016gl068721

Corbi, F., Rivalta, E., Pinel, V., Maccaferri, F., Bagnardi, M., & Acocella, V. (2015). How caldera collapse shapes the shallow emplacement and transfer of magma in active volcanoes. *Earth and Planetary Science Letters*, *431*, 287–293. https://doi.org/10.1016/j.epsl.2015.09.028

Costa, A., Sparks, R., Macedonio, G., & Melnik, O. (2009). Effects of wall-rock elasticity on magma flow in dykes during explosive eruptions. *Earth and Planetary Science Letters*, *288*(3–4), 455–462. https://doi.org/10.1016/j.epsl.2009.10.006

Crouch, S. L., Starfield, A. M., & Rizzo, F. (1983). Boundary element methods in solid mechanics.

Dahm, T. (2000a). Numerical simulations of the propagation path and the arrest of fluid-filled fractures in the Earth. *Geophysical Journal International*, *141*(3), 623–638. https://doi.org/10.1046/j.1365-246x.2000.00102.x

Dahm, T. (2000b). On the shape and velocity of fluid-filled fractures in the Earth. *Geophysical Journal International*, *142*(1), 181–192. https://doi.org/10.1046/j.1365-246x.2000.00148.x

Davis, T., Bagnardi, M., Lundgren, P., & Rivalta, E. (2021). Extreme curvature of shallow magma pathways controlled by competing stresses: Insights from the 2018 Sierra Negra eruption. *Geophysical Research Letters*, *48*(13), e2021GL093038. https://doi.org/10.1029/2021gl093038

Davis, T., Healy, D., Bubeck, A., & Walker, R. (2017). Stress concentrations around voids in three dimensions: The roots of failure. *Journal of Structural Geology*, *102*, 193–207. https://doi.org/10.1016/j.jsg.2017.07.013

Davis, T., Healy, D., & Rivalta, E. (2019). Slip on wavy frictional faults: Is the 3rd dimension a sticking point? *Journal of Structural Geology*, *119*, 33–49. https://doi.org/10.1016/j.jsg.2018.11.009

Davis, T., Rivalta, E., & Dahm, T. (2020). Critical fluid injection volumes for uncontrolled fracture ascent. *Geophysical Research Letters*, *47*(14), e2020GL087774. https://doi.org/10.1029/2020GL087774

Davis, T., Rivalta, E., Smittarello, D., & Katz, R. F. (2023). Ascent rates of 3-D fractures driven by a finite batch of buoyant fluid. *Journal of Fluid Mechanics*, *954*, A12. https://doi.org/10.1017/jfm.2022.986

Dumont, Q., Cayol, V., Froger, J.-L., & Peltier, A. (2022). 22 years of satellite imagery reveal a major destabilization structure at Piton de la Fournaise. *Nature Communications*, *13*(1), 1–11. https://doi.org/10.1038/s41467-022-30109-w

Ebinger, C., Ayele, A., Keir, D., Rowland, J., Yirgu, G., Wright, T., et al. (2010). Length and timescales of rift faulting and magma intrusion: The Afar rifting cycle from 2005 to present. *Annual Review of Earth and Planetary Sciences*, *38*(1), 439–466. https://doi.org/10.1146/annurev-earth-040809-152333

Einarsson, P., & Brandsdottir, B. (1980). Seismological evidence for lateral magma intrusion during the July 1978 deflation of the Krafla volcano in NE-Iceland. *Journal of Geophysics*, *47*(1), 160–165.

Ferrante, G., Rivalta, E., & Maccaferri, F. (2022). Numerical simulation of magma pathways and vent distribution in rifts from the early stages to maturity. *ESS Open Archive*. Authorea Preprints. https://doi.org/10.1002/essoar.10512592.1

Gaete, A., Kavanagh, J. L., Rivalta, E., Hazim, S. H., Walter, T. R., & Dennis, D. J. (2019). The impact of unloading stresses on post-caldera magma intrusions. *Earth and Planetary Science Letters*, *508*, 109–121. https://doi.org/10.1016/j.epsl.2018.12.016

Geshi, N., Yamada, I., Matsumoto, K., Nishihara, A., & Miyagi, I. (2020). Accumulation of rhyolite magma and triggers for a caldera-forming eruption of the Aira Caldera, Japan. *Bulletin of Volcanology*, *82*(6), 1–18. https://doi.org/10.1007/s00445-020-01384-6

Gómez-Vasconcelos, M. G., Villamor, P., Cronin, S. J., Palmer, A., Procter, J., & Stewart, R. B. (2020). Spatio-temporal associations between dike intrusions and fault ruptures in the Tongariro Volcanic Center, New Zealand. *Journal of Volcanology and Geothermal Research*, *404*, 107037. https://doi.org/10.1016/j.jvolgeores.2020.107037

Grosfils, E. B., McGovern, P. J., Gregg, P. M., Galgana, G. A., Hurwitz, D. M., Long, S. M., & Chestler, S. R. (2015). Elastic models of magma reservoir mechanics: A key tool for investigating planetary volcanism. *Geological Society, London, Special Publications*, *401*(1), 239–267. https://doi.org/10.1144/sp401.2

Gudmundsson, A. (2002). Emplacement and arrest of sheets and dykes in central volcanoes. *Journal of Volcanology and Geothermal Research*, *116*(3–4), 279–298. https://doi.org/10.1016/s0377-0273(02)00226-3

Gudmundsson, A. (2006). How local stresses control magma-chamber ruptures, dyke injections, and eruptions in composite volcanoes. *Earth-Science Reviews*, *79*(1–2), 1–31. https://doi.org/10.1016/j.earscirev.2006.06.006

Gudmundsson, M. T., Jónsdóttir, K., Hooper, A., Holohan, E. P., Halldórsson, S. A., Ófeigsson, B. G., et al. (2016). Gradual caldera collapse at Bárdarbunga volcano, Iceland, regulated by lateral magma outflow. *Science*, *353*(6296), aaf8988. https://doi.org/10.1126/science.aaf8988

Heimisson, E. R., Hooper, A., & Sigmundsson, F. (2015). Forecasting the path of a laterally propagating dike. *Journal of Geophysical Research: Solid Earth*, *120*(12), 8774–8792. https://doi.org/10.1002/2015jb012402

Hildreth, W. (2004). Volcanological perspectives on Long Valley, Mammoth Mountain, and Mono Craters: Several contiguous but discrete systems. *Journal of Volcanology and Geothermal Research*, *136*(3–4), 169–198. https://doi.org/10.1016/j.jvolgeores.2004.05.019

Hildreth, W., Fierstein, J., & Calvert, A. (2017). Early postcaldera rhyolite and structural resurgence at Long Valley Caldera, California. *Journal of Volcanology and Geothermal Research*, *335*, 1–34. https://doi.org/10.1016/j.jvolgeores.2017.01.005

Ito, G., & Martel, S. J. (2002). Focusing of magma in the upper mantle through dike interaction. *Journal of Geophysical Research*, *107*(B10), ECV-6–ECV6-17. https://doi.org/10.1029/2001jb000251

Jaeger, J., Cook, N., & Zimmermann, R. (2007). *Fundamentals of rock mechanics*. Blackwell.

Johnson, N. L., Kotz, S., & Balakrishnan, N. (1994). Beta distributions. In *Continuous univariate distributions* (2nd ed., pp. 221–235). John Wiley and Sons.

Kühn, D., & Dahm, T. (2008). Numerical modelling of dyke interaction and its influence on oceanic crust formation. *Tectonophysics*, *447*(1–4), 53–65. https://doi.org/10.1016/j.tecto.2006.09.018

Le Corvec, N., Menand, T., & Lindsay, J. (2013). Interaction of ascending magma with pre-existing crustal fractures in monogenetic basaltic volcanism: An experimental approach. *Journal of Geophysical Research: Solid Earth*, *118*(3), 968–984. https://doi.org/10.1002/jgrb.50142

Lister, J. R., & Kerr, R. C. (1991). Fluid-mechanical models of crack propagation and their application to magma transport in dikes. *Journal of Geophysical Research*, *96*(B6), 10049–10077. https://doi.org/10.1029/91jb00600

Maccaferri, F., Bonafede, M., & Rivalta, E. (2010). A numerical model of dyke propagation in layered elastic media. *Geophysical Journal International*, *180*(3), 1107–1123. https://doi.org/10.1111/j.1365-246X.2009.04495.x

Maccaferri, F., Bonafede, M., & Rivalta, E. (2011). A quantitative study of the mechanisms governing dike propagation, dike arrest and sill formation. *Journal of Volcanology and Geothermal Research*, *208*(1–2), 39–50. https://doi.org/10.1016/j.jvolgeores.2011.09.001

Maccaferri, F., Richter, N., & Walter, T. R. (2017). The effect of giant lateral collapses on magma pathways and the location of volcanism. *Nature Communications*, *8*(1), 1–11. https://doi.org/10.1038/s41467-017-01256-2

Maccaferri, F., Rivalta, E., Keir, D., & Acocella, V. (2014). Off-rift volcanism in rift zones determined by crustal unloading. *Nature Geoscience*, *7*(4), 297–300. https://doi.org/10.1038/ngeo2110

Maccaferri, F., Rivalta, E., Passarelli, L., & Aoki, Y. (2016). On the mechanisms governing dike arrest: Insight from the 2000 Miyakejima dike injection. *Earth and Planetary Science Letters*, *434*, 64–74. https://doi.org/10.1016/j.epsl.2015.11.024

Maccaferri, F., Smittarello, D., Pinel, V., & Cayol, V. (2019). On the propagation path of magma-filled dikes and hydrofractures: The competition between external stress, internal pressure, and crack length. *Geochemistry, Geophysics, Geosystems*, *20*(4), 2064–2081. https://doi.org/10.1029/2018GC007915

MacLeod, N. S., Sherrod, D. R., Chitwood, L. A., & Jensen, R. A. (1982). *Geologic map of Newberry Volcano, Deschutes, Klamath, and Lake Counties, Oregon*. Geological Survey.

Maerten, F., Maerten, L., Plateaux, R., & Cornard, P. (2022). *Joint inversion of tectonic stress and magma pressures using dyke trajectories* (Tech. Rep.). Copernicus Meetings.

Mantiloni, L., Davis, T., Gaete Rojas, A. B., & Rivalta, E. (2021). Stress inversion in a gelatin box: Testing eruptive vent location forecasts with analog models. *Geophysical Research Letters*, *48*(6), e2020GL090407. https://doi.org/10.1029/2020gl090407

Mantiloni, L., Rivalta, E., & Davis, T. (2023). *Sam: Simplified analytical model of dyke pathways in three dimensions*. GFZ. https://doi.org/10.5880/GFZ.2.1.2023.001

Martel, S. J., & Muller, J. R. (2000). A two-dimensional boundary element method for calculating elastic gravitational stresses in slopes. *Pure and Applied Geophysics*, *157*(6–8), 989–1007. https://doi.org/10.1007/s000240050014

Martí, J., Becerril, L., & Rodríguez, A. (2022). How long-term hazard assessment may help to anticipate volcanic eruptions: The case of La Palma eruption 2021 (Canary Islands). *Journal of Volcanology and Geothermal Research*, *431*, 107669. https://doi.org/10.1016/j.jvolgeores.2022.107669

McGarr, A., & Gay, N. (1978). State of stress in the Earth's crust. *Annual Review of Earth and Planetary Sciences*, *6*(1), 405–436. https://doi.org/10.1146/annurev.ea.06.050178.002201

McGuire, W., & Pullen, A. (1989). Location and orientation of eruptive fissures and feeder dykes at Mount Etna; influence of gravitational and regional tectonic stress regimes. *Journal of Volcanology and Geothermal Research*, *38*(3–4), 325–344. https://doi.org/10.1016/0377-0273(89)90046-2

McKenzie, D. (1978). Some remarks on the development of sedimentary basins. *Earth and Planetary Science Letters*, *40*(1), 25–32. https://doi.org/10.1016/0012-821x(78)90071-7

McTigue, D. F., & Mei, C. C. (1981). Gravity-induced stresses near topography of small slope. *Journal of Geophysical Research*, *86*(B10), 9268–9278. https://doi.org/10.1029/jb086ib10p09268

McTigue, D. F., & Mei, C. C. (1987). Gravity-induced stresses near axisymmetric topography of small slope. *International Journal for Numerical and Analytical Methods in Geomechanics*, *11*(3), 257–268. https://doi.org/10.1002/nag.1610110304

Möri, A., & Lecampion, B. (2022). Three-dimensional buoyant hydraulic fractures: Constant release from a point source. *Journal of Fluid Mechanics*, *950*, A12. https://doi.org/10.1017/jfm.2022.800

Müller, B., Zoback, M. L., Fuchs, K., Mastin, L., Gregersen, S., Pavoni, N., et al. (1992). Regional patterns of tectonic stress in Europe. *Journal of Geophysical Research*, *97*(B8), 11783–11803. https://doi.org/10.1029/91jb01096

Muller, J. R., Ito, G., & Martel, S. J. (2001). Effects of volcano loading on dike propagation in an elastic half-space. *Journal of Geophysical Research*, *106*(B6), 11101–11113. https://doi.org/10.1029/2000JB900461

Muller, O. H., & Pollard, D. D. (1977). The stress state near Spanish Peaks, Colorado determined from a dike pattern. *Pure and Applied Geophysics*, *115*(1–2), 69–86. https://doi.org/10.1007/bf01637098

Nakada, S., Nagai, M., Kaneko, T., Nozawa, A., & Suzuki-Kamata, K. (2005). Chronology and products of the 2000 eruption of Miyakejima volcano, Japan. *Bulletin of Volcanology*, *67*(3), 205–218. https://doi.org/10.1007/s00445-004-0404-4

Neri, M., Rivalta, E., Maccaferri, F., Acocella, V., & Cirrincione, R. (2018). Etnean and Hyblean volcanism shifted away from the Malta escarpment by crustal stresses. *Earth and Planetary Science Letters*, *486*, 15–22. https://doi.org/10.1016/j.epsl.2018.01.006

Nikkhoo, M., & Walter, T. R. (2015). Triangular dislocation: An analytical, artefact-free solution. *Geophysical Journal International*, *201*(2), 1119–1141. https://doi.org/10.1093/gji/ggv035

Orsi, G., De Vita, S., & Di Vito, M. (1996). The restless, resurgent Campi Flegrei nested caldera (Italy): Constraints on its evolution and configuration. *Journal of Volcanology and Geothermal Research*, *74*(3–4), 179–214. https://doi.org/10.1016/s0377-0273(96)00063-7

Pansino, S., Emadzadeh, A., & Taisne, B. (2022). Modeling dike propagation in both vertical length and horizontal breadth. *Journal of Geophysical Research: Solid Earth*, *127*(10), e2022JB024593. https://doi.org/10.1029/2022jb024593

Pansino, S., & Taisne, B. (2019). How magmatic storage regions attract and repel propagating dikes. *Journal of Geophysical Research: Solid Earth*, *124*(1), 274–290. https://doi.org/10.1029/2018jb016311

Patrick, M. R., Houghton, B. F., Anderson, K. R., Poland, M. P., Montgomery-Brown, E., Johanson, I., et al. (2020). The cascading origin of the 2018 Kīlauea eruption and implications for future forecasting. *Nature Communications*, *11*(1), 1–13. https://doi.org/10.1038/s41467-020-19190-1

Persson, P.-O., & Strang, G. (2004). A simple mesh generator in Matlab. *SIAM Review*, *46*(2), 329–345. https://doi.org/10.1137/s0036144503429121

Pinel, V., Carrara, A., Maccaferri, F., Rivalta, E., & Corbi, F. (2017). A two-step model for dynamical dike propagation in two dimensions: Application to the July 2001 Etna eruption. *Journal of Geophysical Research: Solid Earth*, *122*(2), 1107–1125. https://doi.org/10.1002/2016jb013630

Pollard, D. D. (1987). Elementary fracture mechanics applied to the structural interpretation of dykes. In *Mafic dyke swarms* (Vol. 34, pp. 5–24).

Pollard, D. D., Fletcher, R. C., & Fletcher, R. C. (2005). *Fundamentals of structural geology*. Cambridge University Press.

Pollard, D. D., & Townsend, M. R. (2018). Fluid-filled fractures in Earth's lithosphere: Gravitational loading, interpenetration, and stable height of dikes and veins. *Journal of Structural Geology*, *109*, 38–54. https://doi.org/10.1016/j.jsg.2017.11.007

Rivalta, E. (2010). Evidence that coupling to magma chambers controls the volume history and velocity of laterally propagating intrusions. *Journal of Geophysical Research*, *115*(B7), B07203. https://doi.org/10.1029/2009jb006922

Rivalta, E., Corbi, F., Passarelli, L., Acocella, V., Davis, T., & Di Vito, M. A. (2019). Stress inversions to forecast magma pathways and eruptive vent location. *Science Advances*, *5*(7), eaau9784. https://doi.org/10.1126/sciadv.aau9784

Rivalta, E., Taisne, B., Bunger, A., & Katz, R. (2015). A review of mechanical models of dike propagation: Schools of thought, results and future directions. *Tectonophysics*, *638*, 1–42. https://doi.org/10.1016/j.tecto.2014.10.003

Roman, A., & Jaupart, C. (2014). The impact of a volcanic edifice on intrusive and eruptive activity. *Earth and Planetary Science Letters*, *408*, 1–8. https://doi.org/10.1016/j.epsl.2014.09.016

Rubin, A. M. (1995). Propagation of magma-filled cracks. *Annual Review of Earth and Planetary Sciences*, *23*(1), 287–336. https://doi.org/10.1146/annurev.ea.23.050195.001443

Rubin, A. M., & Gillard, D. (1998). Dike-induced earthquakes: Theoretical considerations. *Journal of Geophysical Research*, *103*(B5), 10017–10030. https://doi.org/10.1029/97jb03514

Savage, W., Swolfs, H., & Amadei, B. (1992). On the state of stress in the near-surface of the Earth's crust. *Pure and Applied Geophysics*, *138*(2), 207–228. https://doi.org/10.1007/bf00878896

Savage, W., Swolfs, H., & Powers, P. (1985). Gravitational stresses in long symmetric ridges and valleys. In *International journal of rock mechanics and mining sciences & geomechanics abstracts* (Vol. 22, pp. 291–302).

Secor, D. T., Jr., & Pollard, D. D. (1975). On the stability of open hydraulic fractures in the Earth's crust. *Geophysical Research Letters*, *2*(11), 510–513. https://doi.org/10.1029/gl002i011p00510

Segall, P., Cervelli, P., Owen, S., Lisowski, M., & Miklius, A. (2001). Constraints on dike propagation from continuous GPS measurements. *Journal of Geophysical Research*, *106*(B9), 19301–19317. https://doi.org/10.1029/2001jb000229

Sigmundsson, F., Hooper, A., Hreinsdóttir, S., Vogfjörd, K. S., Ófeigsson, B. G., Heimisson, E. R., et al. (2015). Segmented lateral dyke growth in a rifting event at Bárdarbunga volcanic system, Iceland. *Nature*, *517*(7533), 191–195. https://doi.org/10.1038/nature14111

Sigurdsson, H., Carey, S., Alexandri, M., Vougioukalakis, G., Croff, K., Roman, C., et al. (2006). Marine investigations of Greece's Santorini volcanic field. *Eos, Transactions American Geophysical Union*, *87*(34), 337–342. https://doi.org/10.1029/2006eo340001

Slim, M., Perron, J. T., Martel, S. J., & Singha, K. (2015). Topographic stress and rock fracture: A two-dimensional numerical model for arbitrary topography and preliminary comparison with borehole observations. *Earth Surface Processes and Landforms*, *40*(4), 512–529. https://doi.org/10.1002/esp.3646

Smith, V., Isaia, R., & Pearce, N. (2011). Tephrostratigraphy and glass compositions of post-15 kyr Campi Flegrei eruptions: Implications for eruption history and chronostratigraphic markers. *Quaternary Science Reviews*, *30*(25–26), 3638–3660. https://doi.org/10.1016/j.quascirev.2011.07.012

Smittarello, D., Smets, B., Barrière, J., Michellier, C., Oth, A., Shreve, T., et al. (2022). Precursor-free eruption triggered by edifice rupture at Nyiragongo volcano. *Nature*, *609*(7925), 83–88. https://doi.org/10.1038/s41586-022-05047-8

Stephansson, O. (1988). Ridge push and glacial rebound as rock stress generators in Fennoscandia. *Bulletin of the Geological Institutions of the University of Uppsala*, *14*, 39–48.

Tada, H., Paris, P., & Irwin, G. (2000). *American Society of Mechanical Engineers. ASM International. The stress analysis of cracks handbook*. ASME Press: Professional Engineering Publisher, ASM International.

Taisne, B., Tait, S., & Jaupart, C. (2011). Conditions for the arrest of a vertical propagating dyke. *Bulletin of Volcanology*, *73*(2), 191–204. https://doi.org/10.1007/s00445-010-0440-1

Takada, A. (1997). Cyclic flank-vent and central-vent eruption patterns. *Bulletin of Volcanology*, *58*(7), 539–556. https://doi.org/10.1007/s004450050161

Townsend, M., & Huber, C. (2020). A critical magma chamber size for volcanic eruptions. *Geology*, *48*(5), 431–435. https://doi.org/10.1130/g47045.1

Townsend, M. R., Pollard, D. D., & Smith, R. P. (2017). Mechanical models for dikes: A third school of thought. *Tectonophysics*, *703*, 98–118. https://doi.org/10.1016/j.tecto.2017.03.008

Uhira, K., Baba, T., Mori, H., Katayama, H., & Hamada, N. (2005). Earthquake swarms preceding the 2000 eruption of Miyakejima volcano, Japan. *Bulletin of Volcanology*, *67*(3), 219–230. https://doi.org/10.1007/s00445-004-0405-3

Urbani, S., Acocella, V., Rivalta, E., & Corbi, F. (2017). Propagation and arrest of dikes under topography: Models applied to the 2014 Bardarbunga (Iceland) rifting event. *Geophysical Research Letters*, *44*(13), 6692–6701. https://doi.org/10.1002/2017gl073130

Weertman, J. (1971). Theory of water-filled crevasses in glaciers applied to vertical magma transport beneath oceanic ridges. *Journal of Geophysical Research*, *76*(5), 1171–1183. https://doi.org/10.1029/jb076i005p01171

Wright, T. J., Sigmundsson, F., Pagli, C., Belachew, M., Hamling, I. J., Brandsdóttir, B., et al. (2012). Geophysical constraints on the dynamics of spreading centres from rifting episodes on land. *Nature Geoscience*, *5*(4), 242–250. https://doi.org/10.1038/ngeo1428

Xu, W., & Jónsson, S. (2014). The 2007–8 volcanic eruption on Jebel at Tair island (Red Sea) observed by satellite radar and optical images. *Bulletin of Volcanology*, *76*(2), 1–14. https://doi.org/10.1007/s00445-014-0795-9

Zhan, Y., Roman, D. C., Le Mével, H., & Power, J. A. (2022). Earthquakes indicated stress field change during the 2006 unrest of Augustine volcano, Alaska. *Geophysical Research Letters*, *49*(10), e2022GL097958. https://doi.org/10.1029/2022gl097958

Zia, H., & Lecampion, B. (2020). Pyfrac: A planar 3D hydraulic fracture simulator. *Computer Physics Communications*, *255*, 107368. https://doi.org/10.1016/j.cpc.2020.107368

Ziv, A., Rubin, A. M., & Agnon, A. (2000). Stability of dike intrusion along preexisting fractures. *Journal of Geophysical Research*, *105*(B3), 5947–5961. https://doi.org/10.1029/1999jb900410